

CIRCULATION COPY
SUBJECT TO RECALL
IN TWO WEEKS

Experimental Results and Theoretical Analysis
of the Effect of Wavelength on Absorption
and Hot Electron Generation in
Laser-Plasma Interaction

C. Garban-Labaune, E. Fabre, C. Max,
F. Amiranoff, R. Fabbro, J. Virmont, W. C. Mead

This paper was prepared for submittal to
Physics of Fluids

January 16, 1985

Lawrence
Livermore
National
Laboratory

This is a preprint of a paper intended for publication in a journal or proceedings. Since changes may be made before publication, this preprint is made available with the understanding that it will not be cited or reproduced without the permission of the author.

DISCLAIMER

This document was prepared as an account of work sponsored by an agency of the United States Government. Neither the United States Government nor the University of California nor any of their employees, makes any warranty, express or implied, or assumes any legal liability or responsibility for the accuracy, completeness, or usefulness of any information, apparatus, product, or process disclosed, or represents that its use would not infringe privately owned rights. Reference herein to any specific commercial products, process, or service by trade name, trademark, manufacturer, or otherwise, does not necessarily constitute or imply its endorsement, recommendation, or favoring by the United States Government or the University of California. The views and opinions of authors expressed herein do not necessarily state or reflect those of the United States Government or the University of California, and shall not be used for advertising or product endorsement purposes.

**Experimental Results and Theoretical Analysis of the Effect
of Wavelength on Absorption and Hot Electron Generation
in Laser-Plasma Interaction**

C. Garban-Labaune, E. Fabre, C. Max,^{a)} F. Amiranoff,
R. Fabbro, J. Virmont, W. C. Mead^{b)}

**Équipe de Greco Interaction Laser Matière
Laboratoire de Physique Des Milieux Ionisés
Groupe de Recherche du Centre National de la Recherche Scientifique
École Polytechnique
F-91128 Palaiseau Cedex, France**

Recent experiments performed at École Polytechnique on the wavelength scaling of laser light absorption by flat plastic targets are presented and interpreted. The measurements show larger absorption fractions for shorter laser wavelengths, lower laser intensities, and longer laser pulse lengths. These experiments are analyzed using computer hydrodynamics codes, and show that there are two possible physics models consistent with the data:

- 1) Inhibited electron heat flow together with absorption rates higher than those predicted by resonance absorption and inverse bremsstrahlung, or
- 2) Nearly classical heat flow, with no additional enhancement in the absorption rate.

a) University of California, Lawrence Livermore National Laboratory,
Livermore, California 94550, U.S.A.

b) University of California, Los Alamos National Laboratory, Los Alamos,
New Mexico 87545, U.S.A.

INTRODUCTION

The choice of an optimum laser wavelength for laser fusion remains an outstanding issue, both experimentally and theoretically. In particular, from the point of view of laser-plasma coupling, incident wavelengths of the order of $1/3 \mu\text{m}$ to $1/4 \mu\text{m}$ have some strong potential advantages over wavelengths in the 1 to $3 \mu\text{m}$ range. To shed more light on this issue we have carried out a series of experiments comparing laser light absorption at wavelengths of $1.06 \mu\text{m}$, $0.53 \mu\text{m}$, and $0.26 \mu\text{m}$. Results on the effect of laser intensity and pulse duration are given. Theoretical analyses both with simple analytical models and with numerical simulation using two 1D hydrodynamics codes show the strong contribution of inverse bremsstrahlung at short wavelengths which can produce a very high level of absorption and less fast electron production.

I. EXPERIMENTAL SET-UP

Our system is a Neodymium glass rod laser, with a final amplifier of 90 mm diameter. With KDP crystals, we can double the frequency with more than 50% efficiency in energy conversion, and quadruple it with 20% efficiency relative to the fundamental frequency.¹ The energies available at various pulse lengths are 20 J - 100 psec or 100 J - 2.5 nsec at $1.06 \mu\text{m}$; 12 J - 80 psec or 32 J - 2 nsec at $0.53 \mu\text{m}$; 10 J - 160 psec at $0.26 \mu\text{m}$.

We have irradiated plane terphane foils, under normal incidence, using a large aperture ($f/1.2$ at $1.06 \mu\text{m}$ and $0.53 \mu\text{m}$; $f/1$ at $0.26 \mu\text{m}$) focusing lens, in order to be as close as possible to spherical target experimental conditions. The focal spot diameter was determined from X-ray pinhole photographs at 1 - 2 keV and by studying the energy which is not intercepted by spherical targets of variable diameters. We found that 80% of the energy

is deposited within 65 μm for all wavelengths. In all the experiments the best focusing position was used, and was determined as the position giving the highest X-ray emission and backscattering from the plasma, and by careful study of the impacts on burnpaper. We found that the absorption was very reproducible, as long as the target was within $\pm 75 \mu\text{m}$ of the best focusing position. As an example of this effect, Fig. 1 shows the variations of the absorption and backreflection with the focusing position at 1.06 μm - 2.5 nsec. Flux variations are obtained by introducing calibrated attenuators on the incident beam.

The main diagnostic is the total absorption measurement. The absorption is evaluated by separately measuring the energy backreflected into the focusing lens (including specular reflection and backreflection), and the energy which is refracted, reflected or scattered in the remainder of the space not subtended by the lens. The effective aperture of the collecting lens for back-reflection was $f/0.8$.

To measure the refracted and scattered light, we use an Ulbricht sphere,² developed in Garching³ and shown in Fig. 2. This is a plexiglass sphere covered with a perfect diffusing paint. The reflected light from the target is completely diffused in the sphere, and each part of its surface received the same energy which is proportional to the reflection. Each of the four photodiodes, arranged on the sphere as indicated on Fig. 2, gives a measurement of the light intensity in the sphere. The photodiodes are protected from direct light by small discs, and equipped with interference filters and attenuators. The final measurement is deduced from the mean value of the signals of the four photodiodes. By that method, we can eliminate inhomogeneities coming from the holes required for the incident beam and target alignment. The sphere is calibrated by measuring the signals obtained

on the photodiodes when we directly shot in the empty sphere or on a dielectric unfocused mirror at low flux. The responses of the diodes were found to be linear to within 5% with the incident intensity and the same in both cases.

The hot electron temperature was determined in the same experiment with a 10 channel continuum X-ray analyzer and the results are detailed in Ref. 4.

II. EXPERIMENTAL RESULTS

We successively present the experimental results concerning the effect of the laser intensity for the three wavelengths ($1.06 \mu\text{m}$ - $0.53 \mu\text{m}$ - $0.26 \mu\text{m}$) in the short and in the long pulse regimes.

A. Short pulse case.

1. $1.06 \mu\text{m}$ - 100 psec.

Figure 3 shows the variations of backreflection into the focusing optics, reflection in the Ulbricht sphere, and total absorption, with incident flux. The first fact of interest is the almost constant (approximately 22%) backscatter when the incident flux varies by more than four orders of magnitude. Since we are at normal incidence, this value includes specular reflection and stimulated Brillouin backscattering. We deduce that the Brillouin effect is very weak under these conditions and probably saturated at a level below 20%. This can be explained by the very steep density gradient due to short pulse illumination which keeps this instability at a very low level. On the other hand, reflection in the Ulbricht sphere increases when flux is

increased, and becomes larger than backreflection for fluxes higher than 10^{10} W/cm². The total absorption rate is deduced from these two curves and we can separate two regimes:

- At low fluxes, $2 \times 10^{10} < I < 10^{13}$ W/cm², absorption decreases when laser intensity increases. For these low fluxes, inverse bremsstrahlung is the main absorption process, and the decrease of absorption may be associated with two mechanisms: first the increase of electron temperature and secondly steepening of the electron density profile. Increase of electron temperature can be explained by classical variation with incident flux in an isothermal corona, by new heating processes appearing at high flux, and by overheating of the corona in the case of inhibited transport. Inhibition of heat transport, and radiation pressure may modify the corona outflow and steepen the density profile near the critical density where most of the collisional absorption takes place.
- For fluxes between 10^{13} and 2×10^{15} W/cm², collisional absorption is very weak, and the almost constant absorption level (approximately 30% \pm 5%) is probably due to resonance absorption on a nonuniform critical surface with ripples in the density profile and possible magnetic fields.⁵

This level of absorption has been observed by many other laboratories in various conditions and is almost independent

of wavelength. At $1.06 \mu\text{m}$ and 10^{12} W/cm^2 we have measured about 30% absorption, which is in agreement with the Los Alamos results for a broader range of intensities.⁶ A study of the variation of absorption as a function of incidence angle gave us the opportunity to observe the influence of resonance absorption for CO_2 irradiations.⁷

2. $0.53 \mu\text{m} - 80 \text{ psec.}$

Experiments analogous to those at $1.06 \mu\text{m}$ were executed at $0.53 \mu\text{m}$, and results are shown on Fig. 4. As at $1.06 \mu\text{m}$, we observe that the backreflection does not change when flux is varied. It stays very weak, approximately 10%, up to intensities of $2 \times 10^{15} \text{ W/cm}^2$. Stimulated Brillouin backscattering does not occur and energy losses are probably due to refraction.

But the most interesting result is the large increase of absorption at $0.53 \mu\text{m}$ compared to $1.06 \mu\text{m}$ for $I \leq 10^{14} \text{ W/cm}^2$.

This result is still more significant if we go to shorter wavelength.

3. $0.26 \mu\text{m} - 60 \text{ psec.}$

For the same conditions as above, the absorption rates are about $(90\% \pm 5\%)$ for I approximately $4 \times 10^{14} \text{ W/cm}^2$. Losses are equally shared between backscattering and reflection in the sphere, 3 to 5% each. The same absorptions were obtained for several different kinds of materials: plastic, aluminium, copper and gold.

The increase of absorption with shorter wavelength can be explained by the better inverse bremsstrahlung efficiency, first because the laser light penetrates to higher densities where the plasma is more collisional, and secondly because radiation pressure and flux limitation, which produce steepening of the density gradient and which can make the corona hotter, must occur at higher fluxes for short wavelengths. More detailed studies of these effects will be given in Sec. IV.

B. The long pulse case.

Recent studies have shown that it is interesting to use laser pulses of longer duration, in order to shift from the exploding pusher to the ablative compression regime. In the latter case, the electron density profile is smoother, extending further in front of the critical density layer. The associated increase of inverse bremsstrahlung and consequently of total absorption, compared to short pulses, is observed for the three wavelengths at low fluxes. But at high fluxes, effects such as Brillouin scattering can modify this prediction depending on the laser wavelength, and we discuss the three cases separately.

1. 1.06 μm - 2.5 nsec.

Figure 5 shows the detailed reflection and absorption at 1.06 μm versus incident flux. We observe that at low flux, backscattering is almost constant below $5 \times 10^{13} \text{ W/cm}^2$, and is lower than reflection in the Ulbricht sphere. But for fluxes higher than $5 \times 10^{13} \text{ W/cm}^2$, the energy backscattered into the

focusing optics increases very rapidly with the flux, and becomes larger than refraction for $I = 10^{14}$ W/cm². These results suggest that the Brillouin back-scattering instability becomes important in the long pulse regime at 1.06 μ m, for fluxes higher than 10^{14} W/cm². It is reasonable that Brillouin backscatter should dominate over sidescatter for our experiments, since the small focal spot diameter does not provide many growth-lengths in the sideways direction. Correlated with the increased scattering, we see a large decrease of absorption. If we extrapolate the absorption curves, we could expect less absorption at high fluxes with long pulses, as compared with short pulses.

2. 0.53 μ m - 2 nsec.

At 0.53 μ m (Fig. 6), experiments with long pulses confirm the high efficiency of inverse bremsstrahlung, and absorptions larger than 80% are obtained for $I \leq 10^{14}$ W/cm². However the most interesting result in these curves is the very low level of backscatter below 4×10^{14} W/cm² (less than 5%) which shows that Brillouin instability is not efficient below this intensity.

3. 0.26 μ m.

It was not possible to do long pulse experiments at 0.26 μ m because of the low conversion efficiency of the crystals. So in order to study the Brillouin instability, we have carried out experiments with a prepulse containing 10 to 20% of the total energy, 200 ps long and preceeding the main pulse by a variable time delay (540 psec. + 7 nsec.). Detailed results on

the backscattering and the spectra of the backreflected light will be reported elsewhere. To summarize this experiment, for all prepulses, and for main-pulse fluxes about $4 \times 10^{14} \text{ W/cm}^2$, absorptions remain very high (approximately 90%), and backscattering very low ($< 5\%$). So it seems at this flux, that the Brillouin instability is not very efficient. However these results should be extended to higher incident laser fluxes to attain a parameter regime where the Brillouin threshold intensity is exceeded by a large factor.

In conclusion, our experiments, whose results are summarized on Fig. 7, show that absorption increases when laser intensity decreases, and when wavelength decreases. Under conditions where Brillouin scatter is not important, absorption increases for longer pulse durations. Other laboratories⁸ have now obtained absorption measurements very well consistent with these results if we take into account the variations of pulse lengths and target material.

To analyze these data, we have developed a very simple analytical model in order to see the most important effects, and then we have used two 1D hydrodynamics codes to take into account a greater variety of physical processes.

III. ANALYTICAL MODEL

The variation of the experimental absorption with wavelength λ , laser intensity I_0 , and pulse duration τ , are those typical of collisional absorption with these parameters. Thus, we were motivated to develop an analytical model to calculate inverse bremsstrahlung absorption (I.B.) for our

various experimental conditions. We deduce total absorption A by taking into account additional processes which can occur at the critical layer and absorb a fraction α of the laser energy reaching this density. From a theoretical point of view, this fraction represents resonance absorption or parametric instabilities and should lie between 0 and 30% depending on the physical conditions. Thus, the size of α is a parameter of the calculation. The electron temperature T_e is self-consistently determined by assuming that the absorbed energy is used to maintain a self-similar isothermal expansion from the critical surface to the vacuum.⁹

We only consider the short pulse case for which the expansion geometry is quite planar since the axial extent of the plasma is small compared to the focal spot diameter. In this case, Brillouin instability should not be an important part in the energy balance, and we can neglect it in the following. The electron density profile is taken as $n_e/n_c = \exp(-x/L)$ where n_c is the critical density, and L is the density scale length. For a plane isothermal expansion $L = C_s \tau$, where $C_s = (ZT_e/m_e)^{1/2}$ is the ion-acoustic velocity.

The I.B. absorption of the laser light from the vacuum to the critical density, A_1 , can be written as:

$$A_1 = 1 - \exp - \left[\frac{4}{3} \times 11.5 \times \left(\frac{Z_{\text{eff}} \ln \Lambda L \cos^3 \theta}{\lambda^2 T_e^{3/2}} \right) \right]$$

$$= 1 - \exp - \left(0.106 \frac{Z_{\text{eff}} \ln \Lambda \tau \cos^3 \theta}{\lambda^2 T_e} \right)$$

where L and λ are measured in microns, T_e in eV, and τ in psec. Here Z_{eff} is

the mean ion charge defined by $Z_{\text{eff}} = \langle Z^2 \rangle / \langle Z \rangle$, $\ln \Lambda$ is the Coulomb logarithm, and θ the angle of incidence.

Total absorption and electron temperature are then obtained by solving together the following equations:

$$A_{\text{total}} = (\alpha - 1) A_1^2 + 2(1 - \alpha) A_1 + \alpha \quad (1)$$

$$A_1 = 1 - \exp - \left(0.6 \frac{\ln \Lambda}{T_e} \frac{\tau}{\lambda^2} \right) \quad (2)$$

$$\Lambda = 0.84 \lambda T_e \quad (3)$$

$$A I_0 = 4.8 \cdot 10^8 \frac{T_e^{3/2}}{\lambda^2} \quad (4)$$

Equation (4) comes from $A I_0 = 4 n_e C_s^3$ which assumes classical conduction towards the interior of the target and an isothermal outward expansion into the vacuum.⁹

We have numerically solved this system for $\lambda = 0.26 \mu\text{m}$, $\tau = 60 \text{ psec}$; $\lambda = 0.53 \mu\text{m}$, $\tau = 80 \text{ psec}$; and $\lambda = 1.06 \mu\text{m}$, $\tau = 100 \text{ psec}$. We used $Z_{\text{eff}} = 6.25$ corresponding to $\text{C}_{10}\text{H}_8\text{O}_4$. Figure 8 shows the results for $\alpha = 0.2$ and $\alpha = 0.3$.

The results of this model reproduce the major features of our experimental data: absorption increases at shorter wavelength and at lower intensity. It gives good quantitative agreement with our data at $\lambda = 0.53 \mu\text{m}$ and at $\lambda = 0.26 \mu\text{m}$. However, there are two interesting ways in which the model and the data disagree.

- 1) At the lowest intensities for $\lambda = 0.53 \mu\text{m}$ and $1.06 \mu\text{m}$, our analytic model predicts 100% absorption. The experiment showed that absorption saturated at about 75% for $\lambda = 1.06 \mu\text{m}$, and at 75 - 85% for $\lambda = 0.53 \mu\text{m}$. The difference may be due to realistic effects in the experiment such as refraction and departure from a fully-ionized state, or the transient time-development of the blow-off. The latter effect we shall attempt to model in the next section, using hydrodynamics codes.

- 2) At $\lambda = 0.53 \mu\text{m}$ and especially at $1.06 \mu\text{m}$, the slope of the experimental curve is flatter than the prediction of our simple model. Here again, both lack of full ionization and the presence of refraction in the steep gradients at low laser intensity may contribute. An additional effect which can be important at $1.06 \mu\text{m}$ is profile steepening due to radiation pressure or perhaps due to inhibited heat conduction. These will both result in lower inverse bremsstrahlung absorption in the corona.

IV. NUMERICAL SIMULATIONS

For our hydrodynamics simulations, we emphasize laser pulse lengths between 60 and 100 psec. For these pulse lengths the plasma expansion should remain one-dimensional, given the laser spot diameters used in the experiments (50 - 70 μm). This is because the criterion for locally planar behavior is that the expansion speed times the pulse length be less than the spot diameter. Given an expansion velocity of $3 \times 10^7 \text{ cm/sec}$, characteristic of a kilovolt electron temperature, this criterion is well satisfied for the spot diameters between 50 and 70 μm and pulse lengths between 60 and 100 psec. Thus, the curvature of the critical surface should not be important in this short-pulse regime.

Short laser pulses have the additional interpretational advantage that stimulated Brillouin scattering is not an important part of the energy balance, as we saw in Sec. II. We shall compare our computer simulation results with the short-pulse absorption data presented in Sec. II, and also with short-pulse X-ray spectral data for $h\nu = 1 - 20$ keV obtained under these same experimental conditions. A detailed description of the hard X-ray data is presented elsewhere.⁴

To analyze these data, we have used two computer hydrodynamics codes: FILM and LASNEX. FILM, developed by J. Virmont and colleagues,¹⁰ is a Lagrangian, one-dimensional hydrodynamics code. It was used here in planar geometry, with a fully-ionized, perfect-gas equation of state. Hot electrons created by resonance absorption at the critical density surface are transported in a multi-group fashion: flux-limited diffusion in the dense part of the target is matched to a collisionless treatment of the outer coronal regions, as described by Shvarts, et al.¹⁰ The source hot-electron temperature at the peak of the pulse was a specified input parameter T_h . Before and after the peak of the pulse, the source hot-electron temperature varied with laser intensity I_L as $T_h(t) = [I_L(t)/I_{\max}]^{0.4}$.

In the FILM calculations described here, there was no ponderomotive force, and the laser beam had a gaussian temporal shape. The inverse bremsstrahlung absorption was calculated using a mean ion charge defined by $Z_{\text{eff}} = \langle Z^2 \rangle / \langle Z \rangle$, where the relevant mean charge for the hydrodynamics was $\langle Z \rangle$. The inverse bremsstrahlung absorption coefficient was the usual classical, linear value. The target material was plastic, $C_{10}H_8O_4$, $\langle Z \rangle = 4.6$. Targets were 20 - 50 μm thick, and were extended in their transverse dimensions.

In the FILM calculations, there was no inhibition of the suprathermal electron transport. We therefore were left with three free input parameters:

1) The hot-electron temperature T_h was chosen to reproduce the slope of the hard X-ray spectrum. This choice was unambiguous, in the absence of inhibition of the suprathermals.

2) The second input parameter was the fraction of the laser energy reaching critical that was put into the hot-electron distribution. From a theoretical point of view, this fraction represents resonance absorption, and should lie between 15 - 30% as long as the laser intensity is high enough. For low laser intensities (e.g., $I_L < 10^{13}$ W/cm² at 1.06 μ m laser wavelength), resonance absorption is presumed to heat primarily the thermal electron population.¹¹ This latter phenomenon was modeled by dumping a prescribed fraction of the energy reaching critical into the thermal-electron population there.

3) The third free parameter was the flux-limit applied to thermal-electron heat transport. The conductive heat flux was taken to be

$$\vec{q} = \min \{ -\kappa \nabla T_e, -0.6 f n_e m_e v_{te}^3 \nabla T_e / |\nabla T_e| \}, \quad (5)$$

where κ is the classical conductivity¹², T_e , m_e and n_e are the electron temperature, mass, and density, and $v_{te} = (T_e/m_e)^{1/2}$ is the electron thermal speed. The quantity f in Eq. (5) is the flux-limit, and is a phenomenological parametrization of the many different physical processes which seem capable of inhibiting electron heat flow in laser-produced plasmas.¹³ The numerical

algorithm for electron conduction was similar to the new algorithm described in Ref. 14. Note the factor of 0.6 in front of f in Eq. (5).

To obtain a feeling for the difference between different computer hydrodynamics codes, we have also performed analogous computer hydrodynamics simulations using the code LASNEX, developed by G. Zimmerman and colleagues.¹⁵ We regard the differences between the two independently developed codes LASNEX and FILM as representing the "error bars" of the computer calculations. As used here, the physics model in LASNEX was very similar to that described above for FILM, with the following minor exceptions: 1) The ionization state was described by a more complete model, either local thermodynamic equilibrium (LTE) or a non-LTE rate-equation calculation. LASNEX gave similar results in both cases; each was close to full ionization. 2) A tabular equation-of-state for plastic was used, instead of the perfect-gas assumption used by FILM. 3) The effect of spherical divergence was modeled by giving the target a gentle radius of curvature, equal to twice the focal-spot diameter. Detailed comparisons showed that this spherical divergence did not have a significant influence, since the laser pulse-length was so short in our experiments and calculations. 4) The details of the numerical algorithm used to calculate the heat flow were a bit different in LASNEX and FILM. For both the FILM and LASNEX calculations, one-half of the actual laser energy was assumed to be incident on a focal spot equal to the half-energy diameter measured in the experiments.

A. Results at 0.27 μm laser wavelength

For this ultraviolet wavelength, the experimentally observed absorption was about 93% at an incident intensity of $2.7 \times 10^{14} \text{ W/cm}^2$, using a 70 μm diameter focal spot. The pulse length was about 60 psec.

Figure 9 shows the absorption fractions calculated by FILM and LASNEX for these conditions, using $T_h = 1.5 \text{ keV}$ and a resonance absorption fraction $\alpha = 20\%$. For FILM, when the flux limit f is varied from 0.05 to 1.0, the predicted total absorption rises from 66% to 94%. (Recall that the flux limit f used here in Eq. (5) is $(0.6)^{-1} = 1.67$ times the flux limit usually encountered in the literature.) A similar curve was obtained using LASNEX, with a predicted absorption of 81% for $f = 0.05$. For both codes, the increased absorption at higher values of f is due to more efficient inverse bremsstrahlung, since the coronal temperatures fall as the flux limit f increases.

At $\lambda_L = 0.27 \mu\text{m}$, the absorption is largely by inverse bremsstrahlung. Consider for example the LASNEX calculation illustrated in Fig. 10, which used $I_L = 2.4 \times 10^{14} \text{ W/cm}^2$ and a flux limit $f = 0.1$. In this calculation, the total absorption was 94%, of which 89% was due to inverse bremsstrahlung. At the peak of the pulse, the coronal temperature was nearly uniform at $T_e = 550 \text{ eV}$, and both this relatively low temperature and the high electron density accessible to ultraviolet laser light favored efficient classical absorption.

The region in Fig. 10 where the absorption rate is large is very narrow, and lies just outside the critical density surface. The full width at half maximum of the absorption peak is only 1 μm . The highly localized absorption is in turn due to the short density gradient scale length:

$$\frac{n_e}{dn_e/dx} \approx 6 \mu\text{m} \approx (ZT_e/M_i)^{1/2} \tau_L,$$

where $\tau_L = 30$ psec is the half-width of the laser pulse, $T_e = 550$ eV is the coronal temperature at the peak of the pulse, and M_i/Z is approximately twice the proton mass. With this short scale-length, good zoning resolution is essential to obtain accurate numerical results. The calculation illustrated in Fig. 10 had 5 zones within the full width at half maximum of the absorption peak, and 16 zones within the full width at 1/5 maximum. Even finer zoning resolution might be desirable for studies of the details of the absorption layer.

We now return to our discussion of Fig. 9 and the overall trends in the absorption data at $\lambda_L = 0.27 \mu\text{m}$. It is evident from Fig. 9 that if inverse bremsstrahlung and resonance absorption are the only two absorption mechanisms present, the thermal flux-limit f cannot be smaller than about 0.1 - 0.2 and still match the observed absorption of 93%.

Alternatively one might want to use a low flux-limit $f = 0.05$, to be consistent with many $\lambda_L = 1.06 \mu\text{m}$ experiments,¹³ and with recent thin-foil experiments at $\lambda_L = 0.27 \mu\text{m}$.¹⁶ In this case, one must postulate an additional mechanism capable of absorbing the difference between the observed 93% and the predicted 65 - 80% absorption for $f = 0.05$. One thus requires an additional process (one example might be ion-acoustic turbulence)¹⁷ which must absorb between 15 - 25% of the incident energy to explain the data. Another effect that may lead to increased absorption is the lateral transport of energy out of the laser spot. If there were large lateral transport, the cooler coronal temperatures which would result might increase the inverse bremsstrahlung absorption fraction. We shall discuss this effect further below.

The experimental and calculated X-ray spectra are illustrated in Fig. 11a, where the dotted line represents the experiments. The black lines represent spectra calculated by FILM using $T_h = 1.5$ keV, and by LASNEX. Figure 11a shows the X-ray spectra predicted by the hydro codes for the case of inhibited transport, $f = 0.05$. FILM and LASNEX predict X-ray fluences that are a factor of 3 - 10 higher than the experimental data, for X-ray energies above about 5 keV. (The FILM spectrum is too low below 5 keV because the code calculates emission using only optically thin bremsstrahlung, which is an adequate representation at the higher photon energies but not in the region below a few keV).

Figure 11b shows the X-ray spectra predicted for higher values of the flux limit. We have chosen to show the values $f = 0.2$ for FILM and $f = 0.1$ for LASNEX, because for each code these correspond to the smallest flux limits giving the observed absorption value of 93% (see Fig. 9). Both codes indicate that about 5% of the incident energy appears in the form of hot electrons. It is clear from Fig. 11b that the hard X-ray data are well reproduced using a flux limit $f = 0.1 - 0.2$. Hence, one set of theoretical assumptions consistent with the absorption and spectral data at $0.27 \mu\text{m}$ laser wavelength is:

- 1) Classical inverse bremsstrahlung absorption
- 2) Roughly 20% of the energy reaching critical is resonantly absorbed into a hot-electron distribution
- 3) No additional absorption mechanisms are indicated
- 4) Suprathermal electron transport is uninhibited
- 5) The thermal-electron flux limit is not small: $f \geq 0.1 - 0.2$.

On the other hand, as we have mentioned before, there is a previous body of data suggesting that the thermal flux limit f may be quite small, of the order $f = 0.05$. Figure 11a shows the predicted X-ray spectrum for $f = 0.05$, assuming no inhibition of suprathermal electron transport. Using a transport model with uninhibited suprathermals, both codes predict a level of hard X-rays that is too high relative to the experiment, as well as an absorption fraction that is too low. Thus, if the flux limit is really as low as $f = 0.05$, the additional physical mechanism needed to explain the high observed absorption should put its energy into thermal rather than suprathermal electrons, to avoid making the predicted hard X-ray spectrum even higher.

B. Results at 0.53 μm laser wavelength

For the case of green laser light, the observed variation of absorption with incident laser intensity allows a more sensitive test of the physics model in FILM and LASNEX. We again assumed in the computer models that there was classical inverse bremsstrahlung absorption, and that 20% of the light energy reaching critical produced fast electrons. We chose a peak hot-electron temperature T_h to reproduce the correct slope of the hard X-ray spectrum, and we varied the assumed value for the thermal flux-limit f . Suprathermal electrons were not inhibited. The laser pulse length was 80 psec, and the focal spot diameter was about 50 μm .

Figure 12 shows the fractional absorption versus incident laser intensity I_L . The triangular points represent the experimental data. The different curves represent FILM and LASNEX calculations at several laser intensities, for flux limits of $f = 0.05$, $f = 0.5$, and $f = 0.6$.

It is clear from Fig. 12 that if the only absorption mechanisms present are inverse bremsstrahlung and resonance absorption, FILM and LASNEX both imply that the thermal heat flow cannot be very inhibited: $f \geq 0.3 - 0.6$. A flux limit of $f = 0.05$ predicts absorptions that are too small by 15 - 25%, particularly at the higher intensities.

If, on the other hand, one argues on the basis of other experiments that heat flux is very inhibited and the flux limit is actually as low as $f = 0.05$, Fig. 12 shows that one is then forced to hypothesize an additional mechanism capable of absorbing 15 - 25% of the incident laser energy. These conclusions about the absorption of green laser light are hence quite similar to our conclusions for ultraviolet light in the previous section.

Comparison of the high-energy X-ray spectra with FILM and LASNEX predictions for green laser light was possible at incident intensities of 4.2×10^{14} and 1.3×10^{15} W/cm², where the best-fit hot electron temperatures were 2 keV and 4 keV, respectively. Figure 13 shows the spectra for 1.3×10^{15} W/cm². The predicted level of hard X-rays was somewhat high for $f = 0.05$; calculations using $f = 0.6$ were in better agreement with the hard X-ray data than were the strongly inhibited cases. However, the differences were not as large as those shown for ultraviolet incident light in Fig. 11. In general, FILM and LASNEX calculations with uninhibited suprathermal electrons indicate that no more than 10 - 15% of the incident energy went into the hot-electron population at these intensities.

C. Results at 1.06 μ m laser wavelength

The experiments for $\lambda_L = 1.06 \mu\text{m}$ used 100 psec pulse lengths and a 60 μm focal spot diameter. Absorption was nearly constant at about 30%, for

incident intensities above $5 \times 10^{13} \text{ W/cm}^2$ (Sec. II). These data suggest that resonance absorption on a steepened and rippled critical surface⁵ could be responsible for most of the absorption in this intensity range, and that inverse bremsstrahlung is small by comparison. Such an interpretation is roughly consistent with FILM and LASNEX calculations of absorption for these intensities. Since inverse bremsstrahlung is weak, total absorption is not very sensitive to the thermal flux limit f .

The hard X-ray spectra, however, raise questions about this simple absorption scenario. The difficulty is that when suprathermal electron transport is not inhibited, both computer codes predict a level of hard X-ray emission that is a factor of 5 - 30 too high, if 20 - 30% of the laser light is assumed to be absorbed by resonance absorption. This is illustrated in Fig. 14, which compares the data at $I_L = 1.3 \times 10^{15} \text{ W/cm}^2$ with hard X-ray spectra calculated by LASNEX using the standard prescription for resonance absorption: 20% of the laser energy reaching the critical surface is dumped into a hot-electron population. The solid curve (a) shows a LASNEX calculation using a flux limit of $f = 0.05$ for the thermal electrons, and $f = 1.0$ for the hot electrons. The predicted X-ray fluence in this case is higher than the data by a factor of 5 - 10.

Studies of hard X-ray spectral variations such as these have led us to two possible absorption models for $1.06 \mu\text{m}$ laser light which seem consistent with the observations.

Model I. The observed absorption is due to 20 - 30% resonance absorption, but the suprathermal electron transport is strongly inhibited. The additional transport inhibition acts to confine hot electrons to the low-density corona where they do not radiate efficiently. Instead, a large fraction of the suprathermal electron energy is presumably lost in the form of

fast-ion acceleration. This type of scenario is supported by recent thin-foil experiments on transport.¹⁶

We have attempted to model this physics in two different ways. Using LASNEX, we have applied a strong flux limiter $f = 0.05$ to the suprathermal electrons, as well as to the thermals. The resulting predicted X-ray spectrum is shown in curve (b) of Fig. 14. Inhibiting the suprathermal electrons helps to lower the predicted spectrum closer to the experimental value, but computer code predictions still lie above the data.

To help develop a further feel for this phenomenon, we have attempted to study the extreme case where coronal electrons are completely blocked from entering the dense part of the target. To crudely model this situation we have used the code FILM in a mode where all the absorbed laser energy is dumped at the critical surface into a strongly flux-limited thermal population of electrons. Figure 15 shows that a very strong flux limit $f = 0.01 - 0.05$ applied to this "thermal" population of hot electrons is sufficient to bring the hard X-ray emission down to the low level observed in the experiment.

We feel that the hypothesis of strongly inhibited hot electron transport is supported by the calculations reported here, but that it must be investigated further using numerical transport models more appropriate to the accurate description of fast-ion losses and hot-electron motions in the corona.¹⁸

Model II. If suprathermal electron transport is not strongly inhibited, comparison of the hard X-ray spectrum with FILM and LASNEX indicates that only 2 - 5% of the incident laser energy is going into a hot-electron population for 1.06 μm laser light. In this case, one would need to postulate an additional mechanism capable of absorbing about 25% of the incident energy into a thermal population of electrons. (Inverse bremsstrahlung is too weak in this high-intensity regime.)

We have briefly studied this alternative using LASNEX, by dumping only 5% of the energy reaching the critical surface into hot electrons.

Simultaneously, the energy absorbed by the thermal electrons was artificially increased, by multiplying the inverse bremsstrahlung absorption coefficient by a factor of two. The resulting total absorption of 21% was thus not too far below the observed value of 25 - 30% at an intensity of 10^{15} W/cm². For this calculation, which is illustrated as curve (c) of Fig. 14, the flux limits were $f = 0.05$ for the thermal electrons and $f = 1.0$ for the suprathermals.

This type of model can also come quite close to matching the observed hard X-ray spectrum (Fig. 14). However, this second model makes us uneasy from a theoretical point of view, because extensive computer simulations¹⁸ show that resonance absorption can readily absorb 20 - 30% of the light reaching the critical surface in this short-pulse parameter regime. For theoretical reasons we tend to favor Model I, because we can think of mechanisms such as megagauss d.c. magnetic fields¹⁹ which would be capable of inhibiting the transport of suprathermal electrons, particularly for 1.06 μ m laser light.

We have also tried to model the $\lambda_L = 1.06$ μ m short-pulse absorption data at low laser intensities, $I_L < 10^{13}$ W/cm². We deposited the energy due to resonance absorption into the thermal electrons, as described in Ref. 11. We found the interesting result that with a resonance absorption fraction $\alpha = 20\%$, FILM predicted absorptions that were larger than those measured experimentally. To match the observed absorption, we had to decrease the resonance absorption fraction to roughly 5% at these low laser intensities. Part of this effect may be due to FILM's lack of a treatment of partial ionization. We remark that interpretations of recent long-pulse

experiments under collisional conditions²⁰ have also found it necessary to reduce the resonance absorption fraction to only a few percent.

D. Discussion

Analysis of the detailed trends of our data using the computer hydrodynamics codes FILM and LASNEX has allowed us to arrive at two alternative physics models consistent with the absorption data and the hard X-ray spectra. Either

1. Transport of both thermal and suprathermal electrons is relatively uninhibited, and the two dominant absorption mechanisms are inverse bremsstrahlung and resonance absorption,

or

2. Thermal transport is very inhibited (as suggested by previous experiments^{13,16}) and there is a further, presently unidentified mechanism capable of absorbing about 15 - 25% of the incident energy.

In addition, our analysis of the X-ray spectra produced by 1.06 μm laser light suggests that in this case hot-electron transport may be strongly inhibited.

These conclusions have inherent limitations, however, and we would like to point out some of them here.

From the experimental point of view, there is uncertainty in the value of the laser pulse length and spot size and, hence, in the appropriate incident laser intensity to use in the computer simulations. Since the predicted absorption fraction depends on intensity, this introduces an uncertainty into our conclusions about the magnitude of the flux limit f and the necessary

additional absorption processes. We can estimate this uncertainty from Fig. 12. If the actual value of the laser intensity were lower than we had thought, the experimental points would shift to the left by an appropriate amount. For example, consider an error of a factor of two in the intensity. In this case, the calculated absorptions for $f = 0.05$ and $f = 0.1$ would still lie well below the measured values, and our conclusions would not be qualitatively changed. However, if the actual value of the intensity were lower by a factor of four or more, our uncertainty would begin to be quite large.

A second question concerns the amount of lateral transport. If a substantial fraction of the incident laser intensity were to be spread out laterally beyond the edge of the focal spot, then one should use an appropriately lower incident laser intensity to model these experiments with a one-dimensional hydrodynamics code. In the code studies reported here this effect was not included, since we had no experimental evidence on the existence or magnitude of such a lateral transport effect. Additional experiments specifically addressing the lateral transport issue would be very desirable.

V. SUMMARY AND CONCLUSIONS

We have reported the results of a scaling study of laser light absorption by solid plastic targets. Using a frequency-multiplied Nd-glass laser, we have measured the absorption at laser wavelengths of 1.06 μm , 0.53 μm , and 0.27 μm . Absorption increases at shorter laser wavelengths, lower laser intensities, and longer laser pulse-lengths. For an ultraviolet laser wavelength $\lambda_L = 0.27 \mu\text{m}$, absorption is nearly total even at a laser intensity of $3 \times 10^{14} \text{ W/cm}^2$.

For a laser pulse length of 2 nsec and a wavelength $\lambda_L = 1.06 \mu\text{m}$, we found evidence suggesting stimulated Brillouin scattering at high laser intensities. This enhanced scattering was not present at the shorter laser wavelengths $\lambda_L = 0.53 \mu\text{m}$ and $0.27 \mu\text{m}$, thus confirming simple theoretical scaling predictions²¹ for Brillouin scatter.

We have interpreted our absorption data using a simple analytic model which includes classical inverse bremsstrahlung, resonance absorption, and an isothermally expanding plasma corona. The model's results agree qualitatively with our short-pulse absorption data, but depart from the data quantitatively in some interesting and suggestive ways.

Detailed computer simulations of our short-pulse experiments lead us to alternative hypotheses about appropriate physics models. Either

- a) The absorption is entirely due to classical inverse bremsstrahlung and 20% resonance absorption at the critical surface, in which case the flux limit is $f = 0.1 - 0.2$; or
- b) There is an additional mechanism capable of absorbing 15 - 25% of the incident laser light. In the latter case, we would deduce a flux limit $f = 0.05$, indicating significant inhibition of electron heat flow. (Recall the non-standard definition of f in Eq. 5.)

We discuss elsewhere⁴ our data on hard X-ray spectra at the three laser wavelengths studied here. Qualitatively, the spectra show significantly lower hard X-ray fluences and temperature at the shorter laser wavelengths $\lambda_L = 0.27 \mu\text{m}$ and $0.53 \mu\text{m}$, indicating a smaller and cooler population of hot electrons. However, we caution that targets of a size contemplated for eventual fusion reactors will have underdense plasmas considerably larger than those produced in the experiments reported here. Because of our relatively small laser focal spot size, we have not addressed

the scaling of processes such as stimulated Raman scattering and the two-plasmon decay instability, which are both potential hot-electron sources in larger underdense plasmas.²¹

The eventual success of short-wavelength lasers for directly driven fusion targets will depend on an adequate resolution of the illumination symmetry issues posed by short-wavelength lasers.²² The symmetry question has recently been addressed experimentally²³ at a laser wavelength of 1.06 μm . Further symmetry experiments at sub-micron wavelengths would be highly desirable, to quantitatively evaluate the trade-off between good plasma-physics coupling and good target symmetry.

ACKNOWLEDGMENT

We gratefully acknowledge the help of M. Weinfeld and A. Michard in performing our experiments. This research was done at the Ecole Polytechnique as part of the GRECO Interaction Laser Matiere, supported by the C.N.R.S. of France. The research of C. E. Max and W. C. Mead was also supported by the U.S. Department of Energy, under contract number W-7405-ENG-48 to the Lawrence Livermore National Laboratory.

REFERENCES

1. C. Loth, D. Bruneau and E. Fabre, App. Optics 19, 7, 1022 (1980).
2. R. Ulbricht, Elektrotechn. Z 21, 595 (1900).
3. R. P. Godwin, P. Sachsenmaier and R. Sigel, Phys. Rev. Lett. 39, 1198 (1977).
4. F. Amiranoff, R. Fabbro, E. Fabre, C. Garban-Labaune and M. Weinfeld, J. de Phys. 43, 1037 (1982).
5. J. J. Thomson, W. L. Kruer, A. B. Langdon, C. E. Max and W. C. Mead, Phys. Fluids 21, 707 (1978); F. David and R. Pellat, Phys. Fluids 23, 1682 (1980).
6. E. L. Lindman, J. de Physique, Coll C6, 38, C6-9 (1977).
7. C. Garban-Labaune, E. Fabre, F. David, J. Maignan, and A. Michard, J. Phys. Lett. 41, L-463 (1980).
8. A.G.M. Maaswinkel, K. Eidmann and R. Sigel, Phys. Rev. Lett. 42, 1625 (1979); A.G.M. Maaswinkel, Opt. Comm. 33, 62 (1980); W. Seka, T. Boehly, R. S. Craxton, L. Forsley, L. Goldman, S. Jacobs, R. Keck, B. Nicholson, R. McCrory, M. Richardson, J. Rizzo, J. Soures and K. Tanaka, Bull. Amer. Phys. Soc. 25, 895 (1980); D. C. Slater, G. E. Busch, G. Charatis, R. R. Johnson, F. J. Mayer, R. J. Schroeder, J. D. Simpson, D. Sullivan, J. A. Tarvin, and C. E. Thomas, Phys. Rev. Lett. 46, 1199 (1981); W. C. Mead, E. M. Campbell, K. Estabrook, R. E. Turner, W. L. Kruer, P.H.Y. Lee, B. Pruett, V. C. Rupert, K. G. Tirsell, G. L. Stradling, F. Ze, C. E. Max, M. D. Rosen and B. F. Lasinski, Phys. Fluids 26, 2316 (1983).
9. P. Mora and R. Pellat, Phys. Fluids 22, 2300 (1979); R. Fabbro, E. Fabre, and C. E. Max, Rapport d'activité 1980, GRECO Interaction Laser-Matiere, Ecole Polytechnique (Palaiseau, France) pp. 107-110.

10. J. Virmont, R. Pellat, and P. Mora, *Phys. Fluids* 21, 567 (1978);
D. Shvarts, C. Jablon, I. B. Bernstein, J. Virmont, and P. Mora, *Nucl. Fusion* 19, 1457 (1979); E. Goldman, *Plasma Phys.* 15, 289 (1977)
11. V. L. Ginzburg, *The Propagation of Electromagnetic Waves in Plasma*, (Addison-Wesley, Reading, 1964), pp. 205-229 and 364-368.
12. L. Spitzer, Jr., *Physics of Fully Ionized Gases*, (Wiley-Interscience, New York, 1964), Sec. 5.5.
13. W. L. Kruer, *Comments on Plasma Physics and Controlled Fusion* 5, 69 (1979).
14. C. E. Max, C. F. McKee, and W. C. Mead, *Phys. Fluids* 23, 1620 (1980).
15. G. B. Zimmerman, Univ. of California Report No. UCRL-74811, 1973 (unpublished); G. B. Zimmerman and W. L. Kruer, *Comments on Plasma Physics and Controlled Fusion* 2, 51 (1975).
16. R. Fabbro, E. Fabre, F. Amiranoff and M. Weinfeld, in *Rapport d' Activite 1979*, GRECO Interaction Laser-Matiere, Ecole Polytechnique (Palaiseau, France), pp. 113-129.
17. R. Faehl and W. L. Kruer, *Phys. Fluids* 20, 55 (1977); W. M. Manheimer, *Phys. Fluids* 20, 265 (1977); D. R. Gray and J. K. Kilkenney, *Plasma Physics* 22, 81 (1980); A. Ng and L. Pitt, *Phys. Rev. Lett.* 40, 873 (1978).
18. K. Estabrook, E. J. Valeo, and W. L. Kruer, *Phys. Fluids* 18, 1151 (1975); J. P. Friedberg, R. W. Mitchell, R. L. Morse, and L. J. Rudinski, *Phys. Rev. Lett.* 28, 795 (1972).
19. J. A. Stamper, K. Papadopoulos, R. N. Sudan, S. O. Dean and E. A. McLean, *Phys. Rev. Lett.* 26, 1012 (1971); D. W. Forslund and J. U. Brackbill, *Bull. Amer. Phys. Soc.* 26, 873 (1981); R. Fabbro and P. Mora, *Phys. Lett.* 90A, 48 (1982).

20. M. D. Rosen, D. W. Phillion, V. C. Rupert, W. C. Mead, W. L. Kruer, J. J. Thomson, H. N. Kornblum, V. W. Slvinsky, G. J. Caporaso, M. J. Boyle, and K. G. Tirsell, *Phys. Fluids* 22, 2020 (1979).
21. C. E. Max and K. G. Estabrook, *Comments on Plasma Physics and Controlled Fusion* 5, 239 (1980); C. E. Max, E. M. Campbell, W. C. Mead, W. L. Kruer, D. W. Phillion, R. E. Turner, B. F. Lasinski, and K. G. Estabrook, in Laser Interaction and Related Plasma Phenomena, Vol. 6, H. Hora and G. H. Miley, editors (Plenum, New York, 1984), p. 507.
22. J. H. Gardner and S. E. Bodner, *Phys. Rev. Lett.* 47, 1137 (1981); S. E. Bodner, *J. Fusion Energy* 1 (1981); C. E. Max, J. D. Lindl, and W. C. Mead, *Nuc. Fusion* 23, 131 (1983).
23. S. P. Obenschain, J. Grun, B. H. Ripin and E. A. McLean, *Phys. Rev. Lett.* 46, 1402 (1981).

FIGURE CAPTIONS

1. Variations of absorption and backreflection with focusing position, at $1.06\ \mu\text{m}$ - 2.5 nsec.
2. Schematics of the 4π calorimetry system, using an Ulbricht sphere.
3. Detailed optical energy balance at $1.06\ \mu\text{m}$ for the short pulse regime.
4. Detailed optical energy balance at $0.53\ \mu\text{m}$ for the short pulse regime.
5. Detailed optical energy balance at $1.06\ \mu\text{m}$ for the long pulse regime.
6. Detailed optical energy balance at $0.53\ \mu\text{m}$ for the long pulse regime.
7. Fractional absorption of laser light versus incident flux for various experimental conditions:
 - Short and long laser pulses at $1.06\ \mu\text{m}$ and $0.53\ \mu\text{m}$ on plane $\text{C}_{10}\text{H}_8\text{O}_4$ targets.
 - Typical error bars are represented by dashed lines at $0.26\ \mu\text{m}$ ($\text{C}_{10}\text{H}_8\text{O}_4$ - 60 psec, Au - 60 psec; $\text{C}_{10}\text{H}_8\text{O}_4$ - 150 psec; Al - 150 psec, Au - 150 psec).
8. Absorption rates calculated by the analytical model.
9. Absorption fractions calculated by FILM (F) and by LASNEX (L), for laser wavelength $\lambda_L = 0.27\ \mu\text{m}$ and incident intensity $I_L = 2.4 \times 10^{14}\ \text{W}/\text{cm}^2$. The horizontal axis represents the flux limit f , normalized as in Eq. (5). The laser pulse length was $\tau_L = 60\ \text{psec}$, with gaussian temporal shape. The computer calculations used a hot-electron temperature $T_h = 1.5\ \text{keV}$, classical inverse bremsstrahlung, and resonance absorption fraction $\alpha = 20\%$. The dashed lines indicate the experimental range for the absorption measurements reported in Sec. II.
10. Profiles of electron density and specific absorption rate at the peak of the laser pulse from a LASNEX calculation at $\lambda_L = 0.27\ \mu\text{m}$, $I_L = 2.4 \times 10^{14}\ \text{W}/\text{cm}^2$, pulse length $\tau_L = 60\ \text{psec}$, flux limit $f = 0.1$. At

densities below $n_c = 1.6 \times 10^{22} \text{ cm}^{-3}$, the density scale length is about $6 \text{ } \mu\text{m}$. The full width at half maximum of the absorption-rate peak is $1 \text{ } \mu\text{m}$.

11. Measured (dotted line) and calculated (solid lines) hard X-ray spectra, for the same experimental conditions as Fig. 9. a) FILM and LASNEX predictions for a flux limit $f = 0.05$; b) FILM prediction for $f = 0.2$ and LASNEX prediction for $f = 0.1$.
12. Fractional absorption vs. incident laser intensity I_L , at laser wavelength $\lambda_L = 0.53 \text{ } \mu\text{m}$. Triangles represent experimental data. Curves represent FILM (F) and LASNEX (L) calculations for flux limits of $f = 0.05$, $f = 0.5$ and $f = 0.6$. Laser pulse length was $\tau_L = 80 \text{ psec}$. The computer calculations assumed classical inverse bremsstrahlung and a resonance absorption fraction $\alpha = 20\%$.
13. Hard X-ray spectrum for laser wavelength $\lambda_L = 0.53 \text{ } \mu\text{m}$, intensity $I_L = 1.3 \times 10^{15} \text{ W/cm}^2$, pulse length $\tau_L = 80 \text{ psec}$. Dotted line represents experimental data. Solid lines show computer calculations with $\alpha = 20\%$ and classical inverse bremsstrahlung absorption, for a flux limit $f = 0.05$, $T_h = 4 \text{ keV}$.
14. Hard X-ray spectrum for laser wavelength $\lambda_L = 1.06 \text{ } \mu\text{m}$, intensity $I_L = 1.3 \times 10^{15} \text{ W/cm}^2$, pulse length $\tau_L = 100 \text{ psec}$, $T_h = 20 \text{ keV}$. Dotted line represents experimental data. Solid curves are LASNEX calculations using different physics assumptions. a) Flux limits $f = 0.05$ for thermal electrons, $f = 1.0$ for suprathermal electrons, resonance absorption fraction $\alpha = 20\%$, classical inverse bremsstrahlung. b) Flux limits $f = 0.05$ for both suprathermal and thermal electrons, $\alpha = 20\%$, classical inverse bremsstrahlung. c) Flux limits $f = 0.05$ for thermal electrons, $f = 1.0$ for suprathermal electrons, $\alpha = 5\%$, inverse bremsstrahlung

absorption coefficient multiplied by two. Calculated absorption values corresponding to these three physics models were: a) 28%, b) 24%, c) 21%. Experimental absorption at this intensity was 25 - 30%.

15. Hard X-ray spectrum for laser wavelength $\lambda_L = 1.06 \mu\text{m}$, laser intensity $I_L = 1.3 \times 10^{15} \text{ W/cm}^2$, pulse length $\tau_L = 100 \text{ psec}$. Dotted line shows experimental data. Solid curves are results of FILM calculations where resonance absorption is assumed to deposit its energy entirely into a flux-limited thermal population of electrons at the critical surface. Calculations are shown for two values of the thermal flux limit f , normalized as in Eq. (5). There are no suprathermal electrons in these calculations.

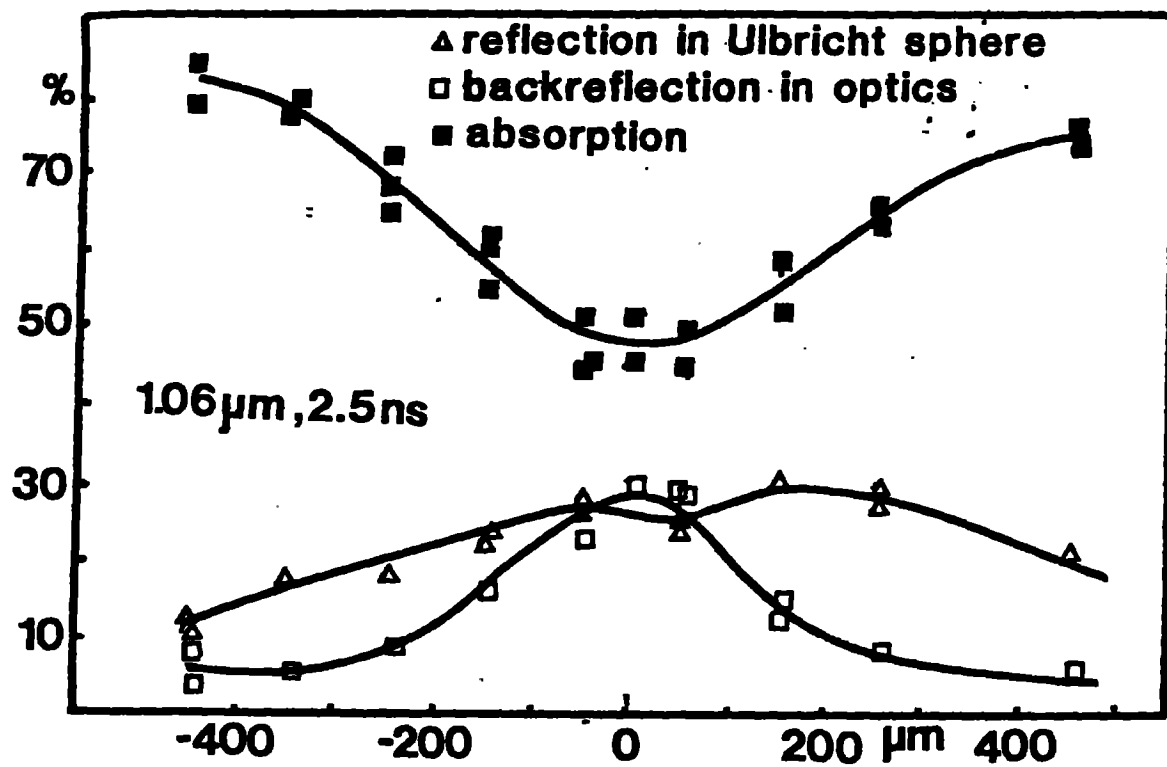


Fig. 1

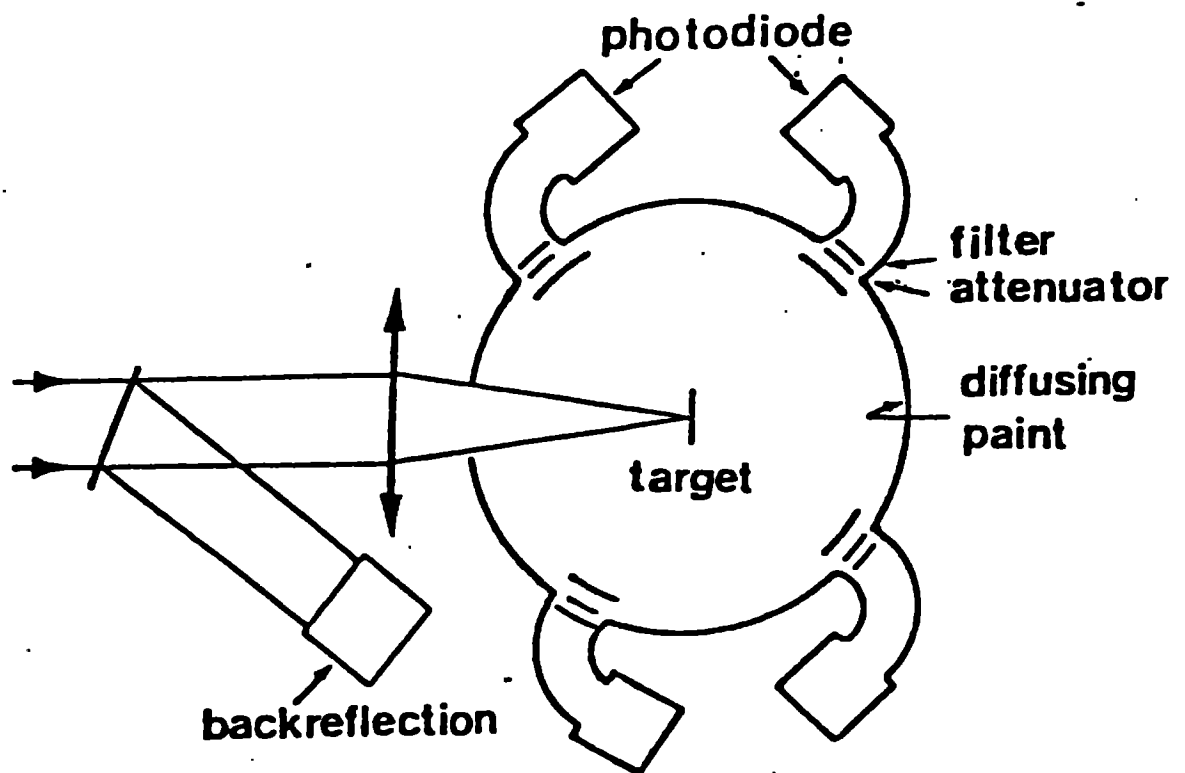


Fig. 2.

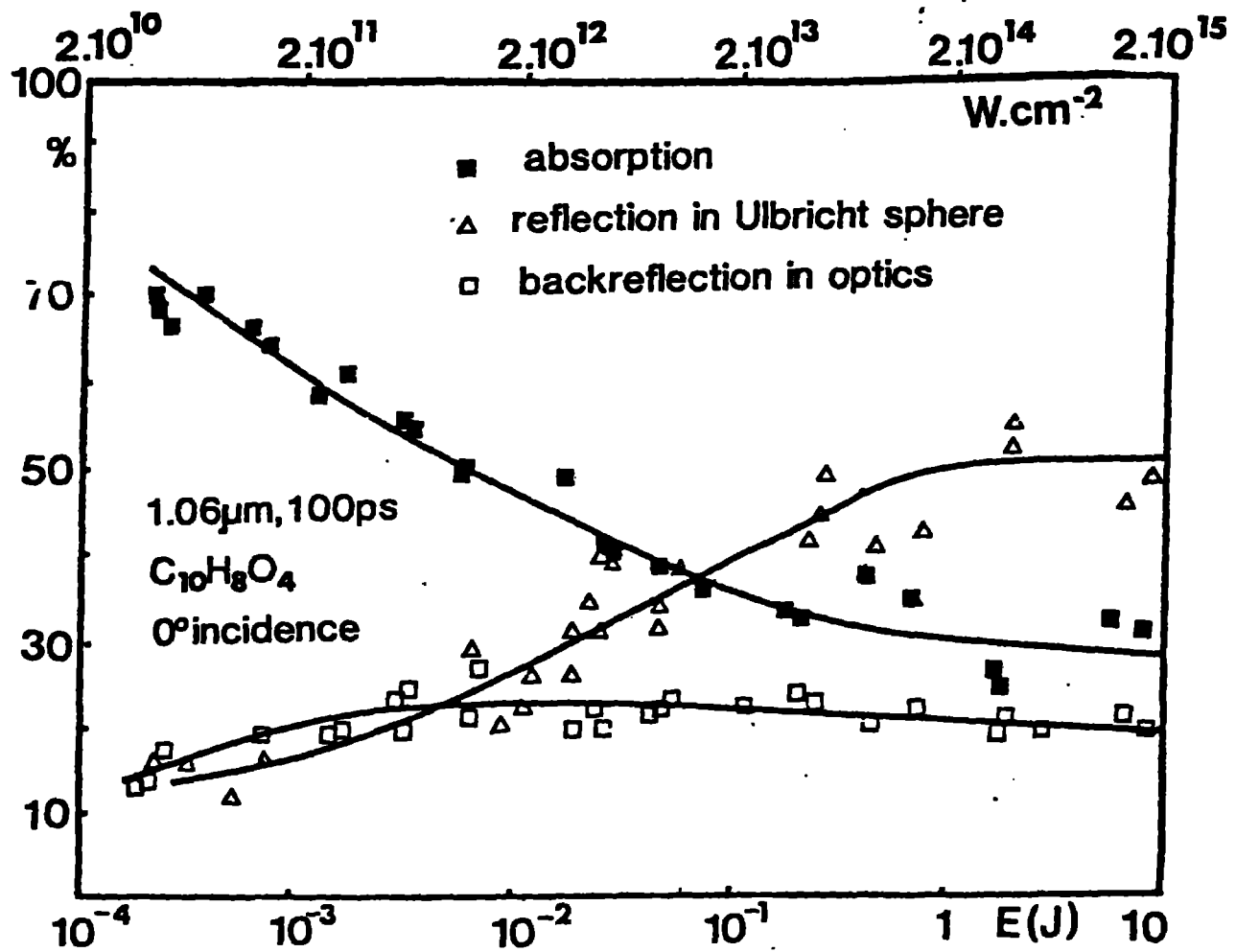


Fig. 3

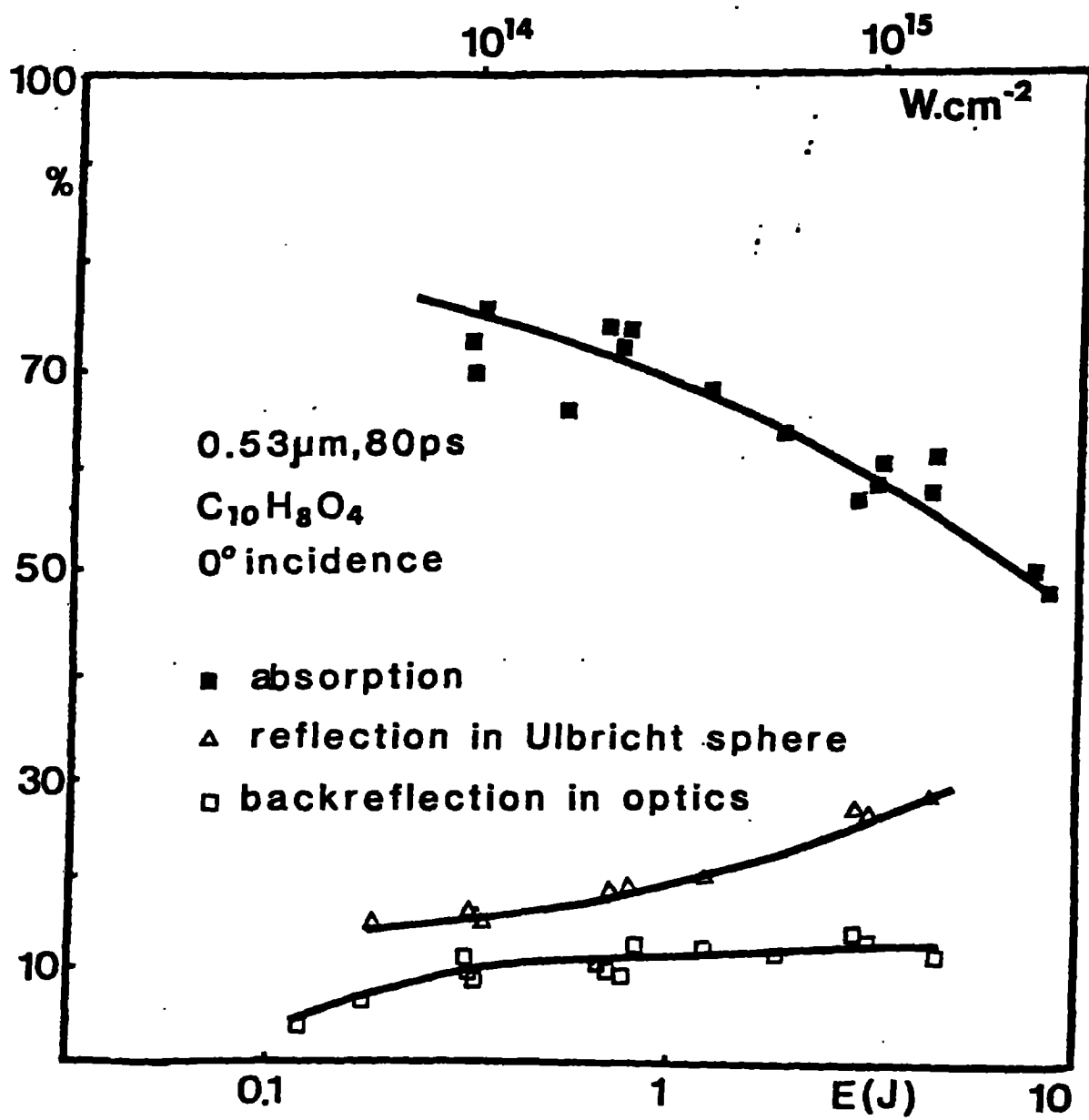


Fig. 4

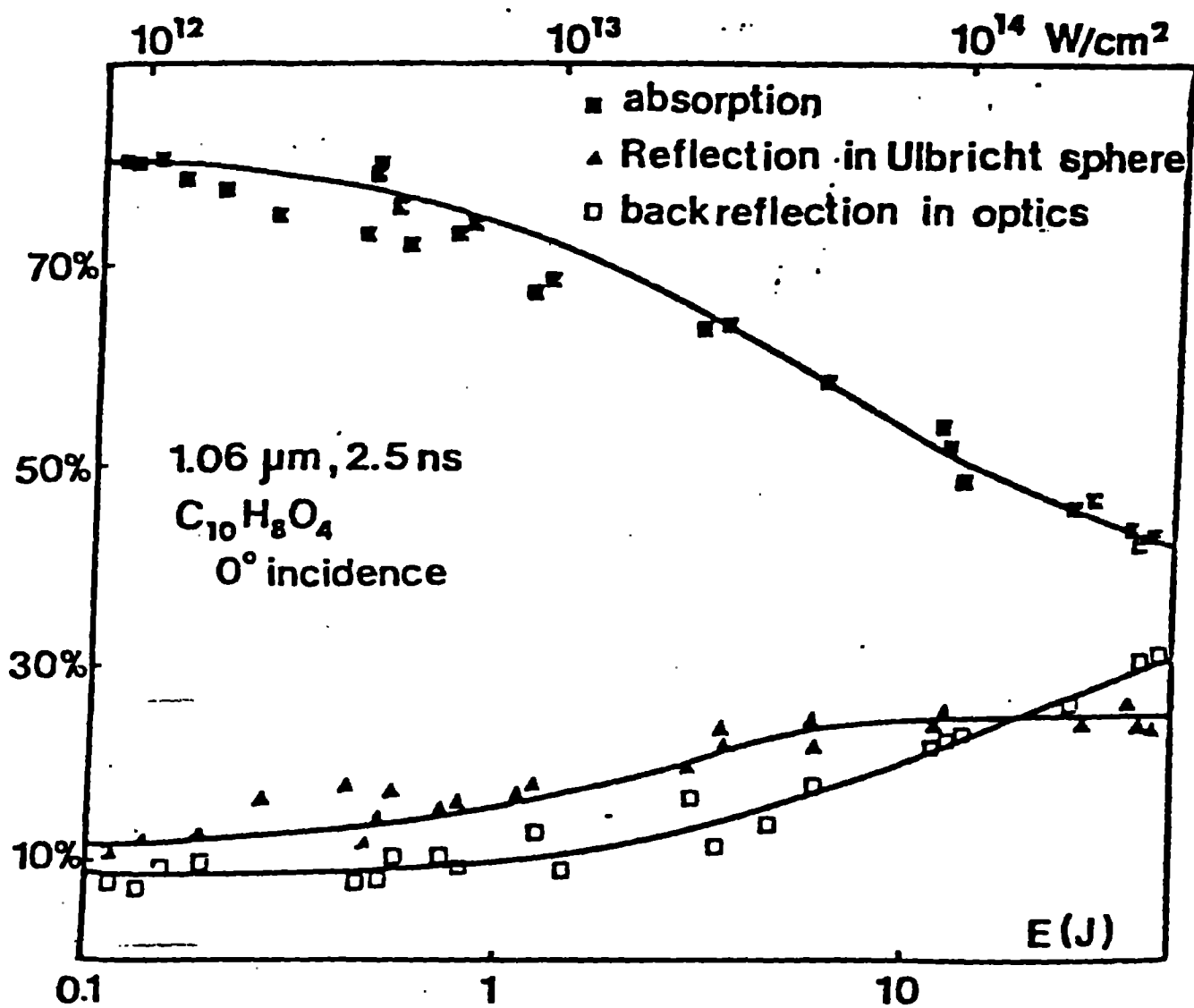


Fig. 5

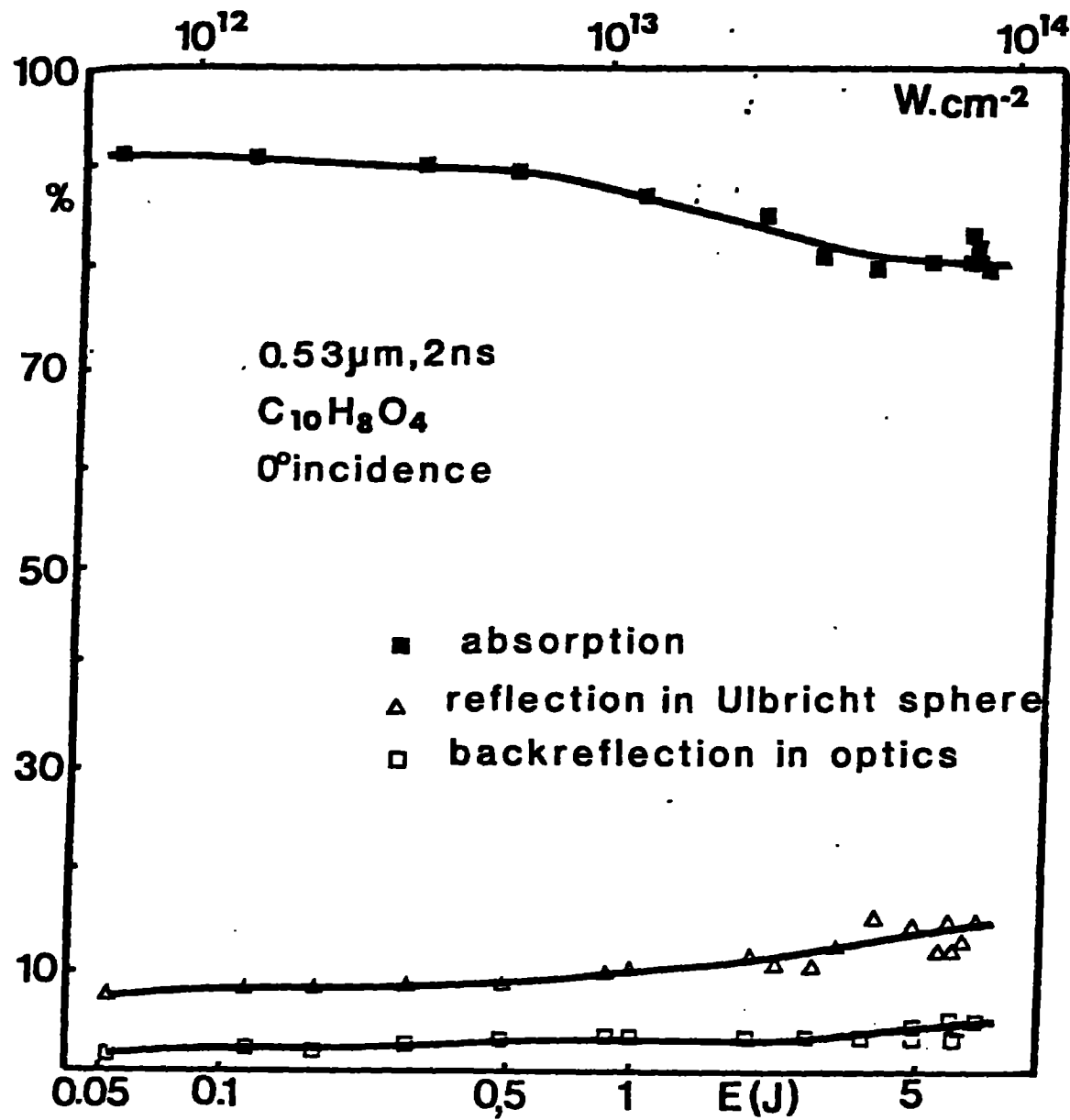


Fig. 6

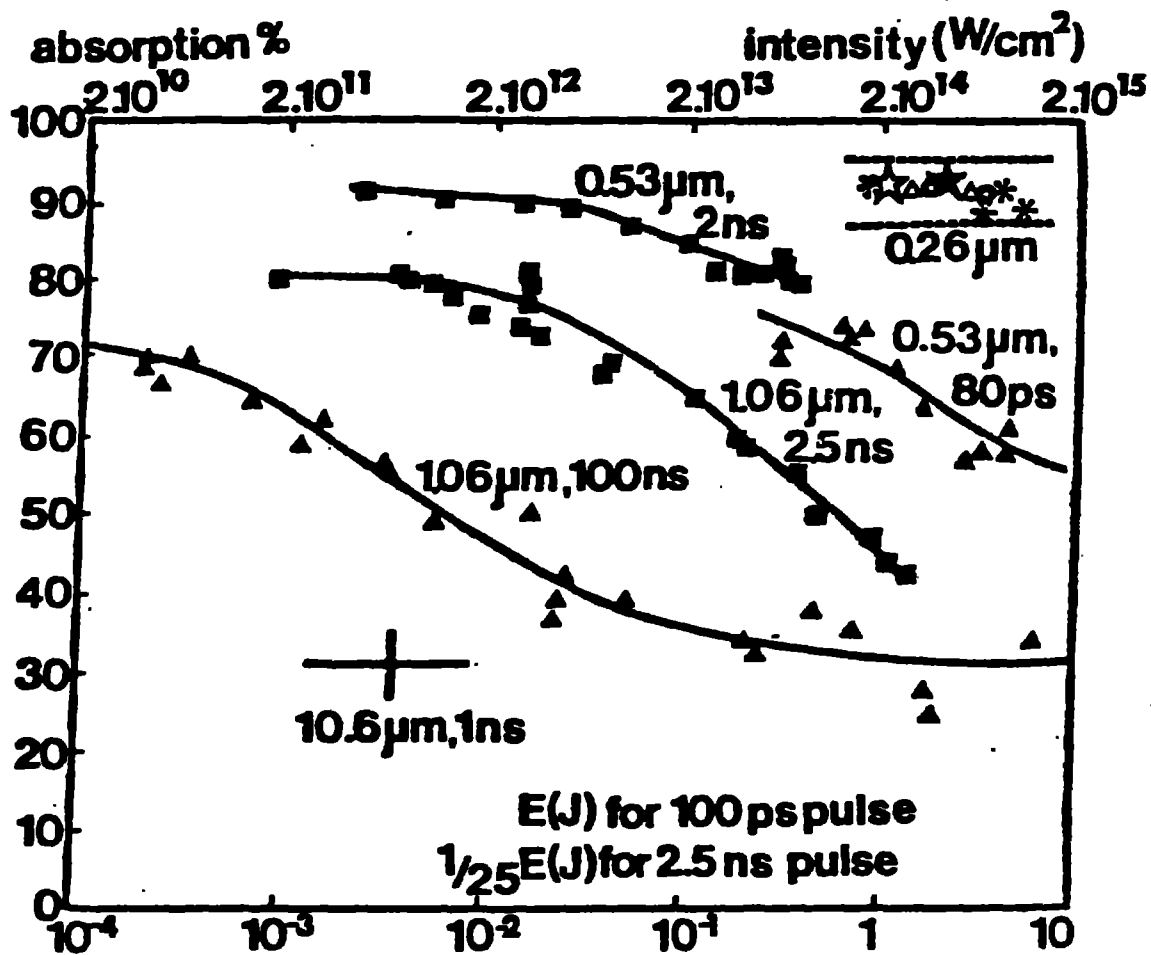


Fig. 7

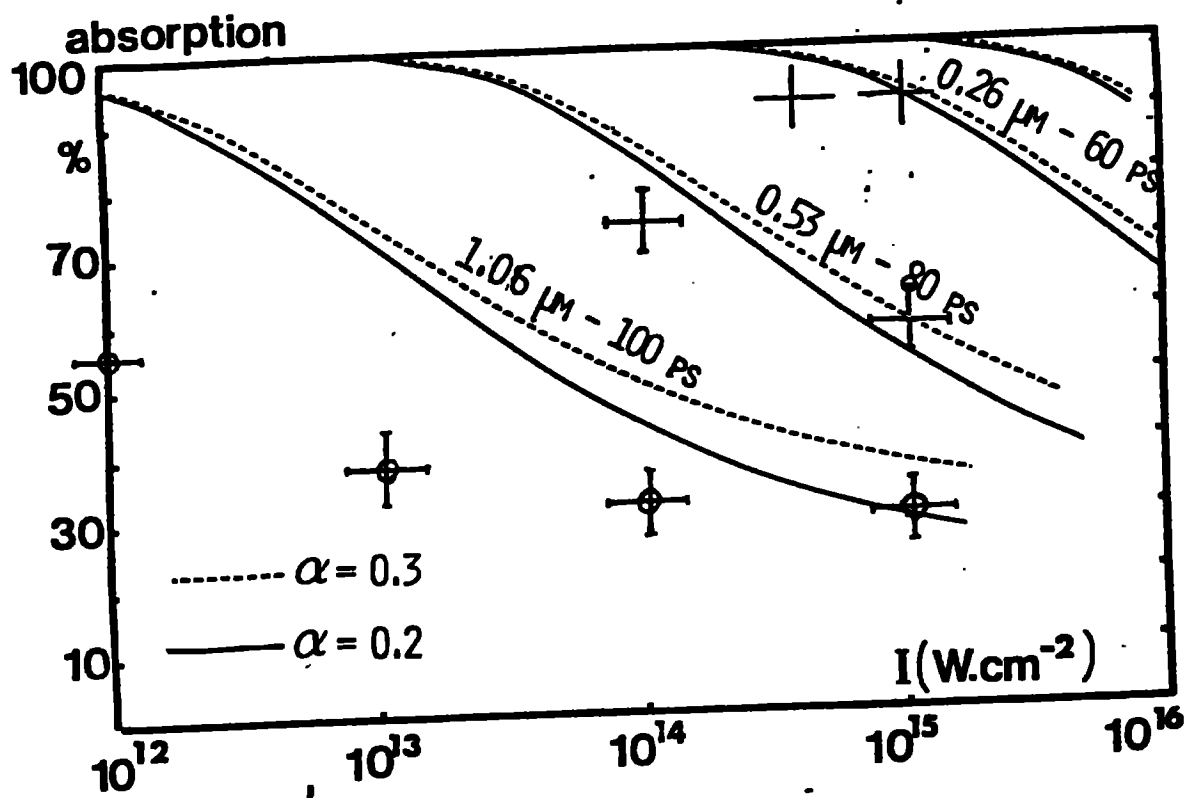


Fig. 8

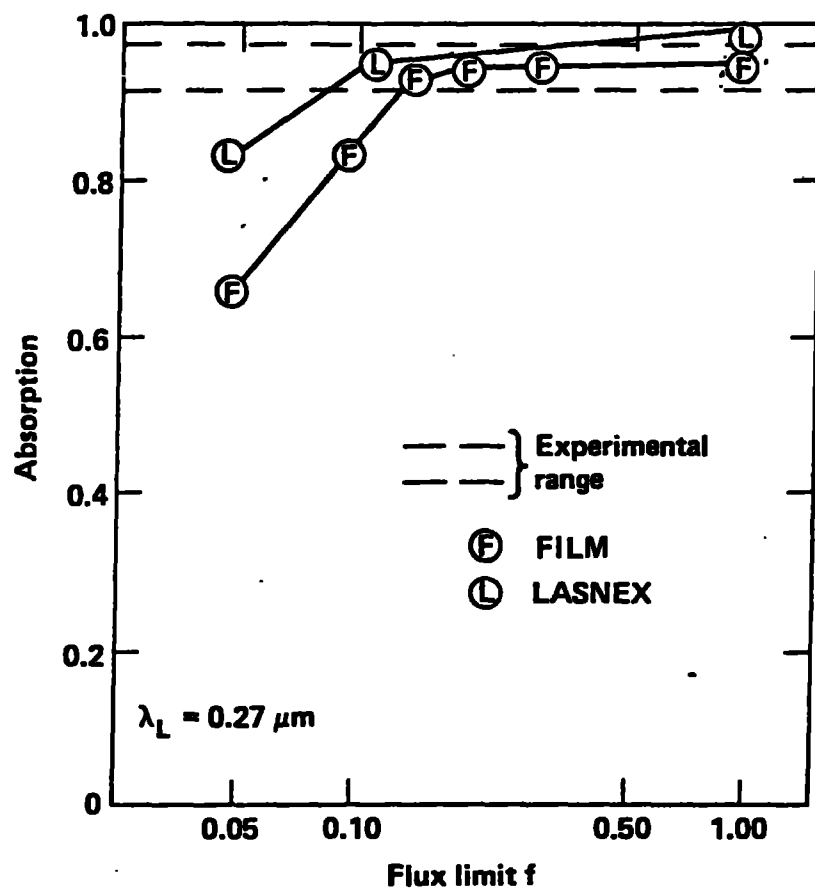


Fig. 9

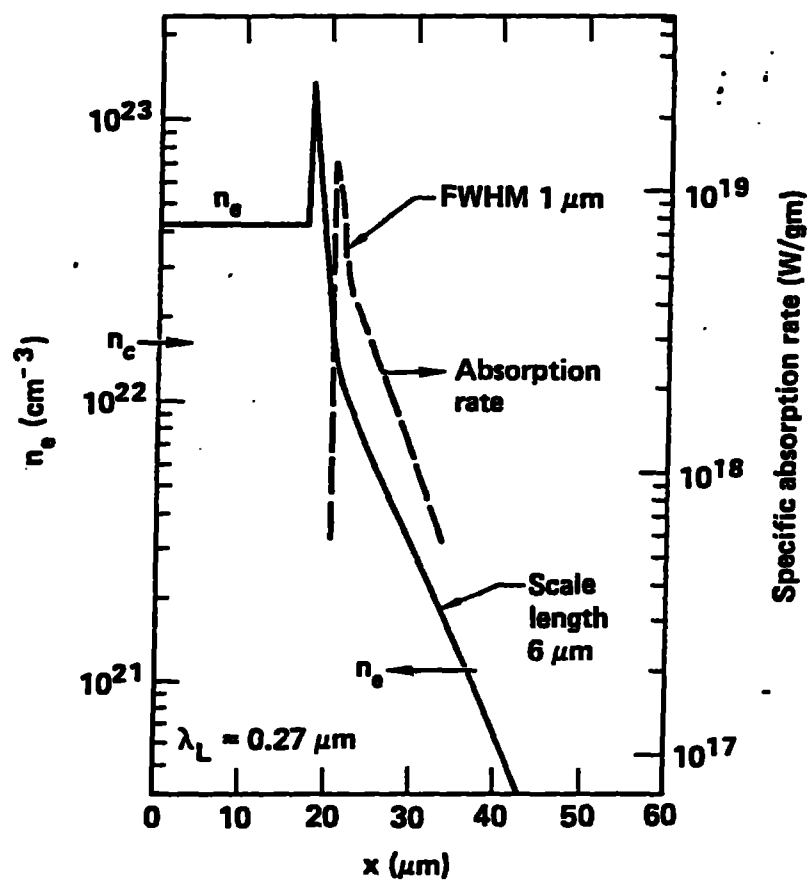


Fig. 10

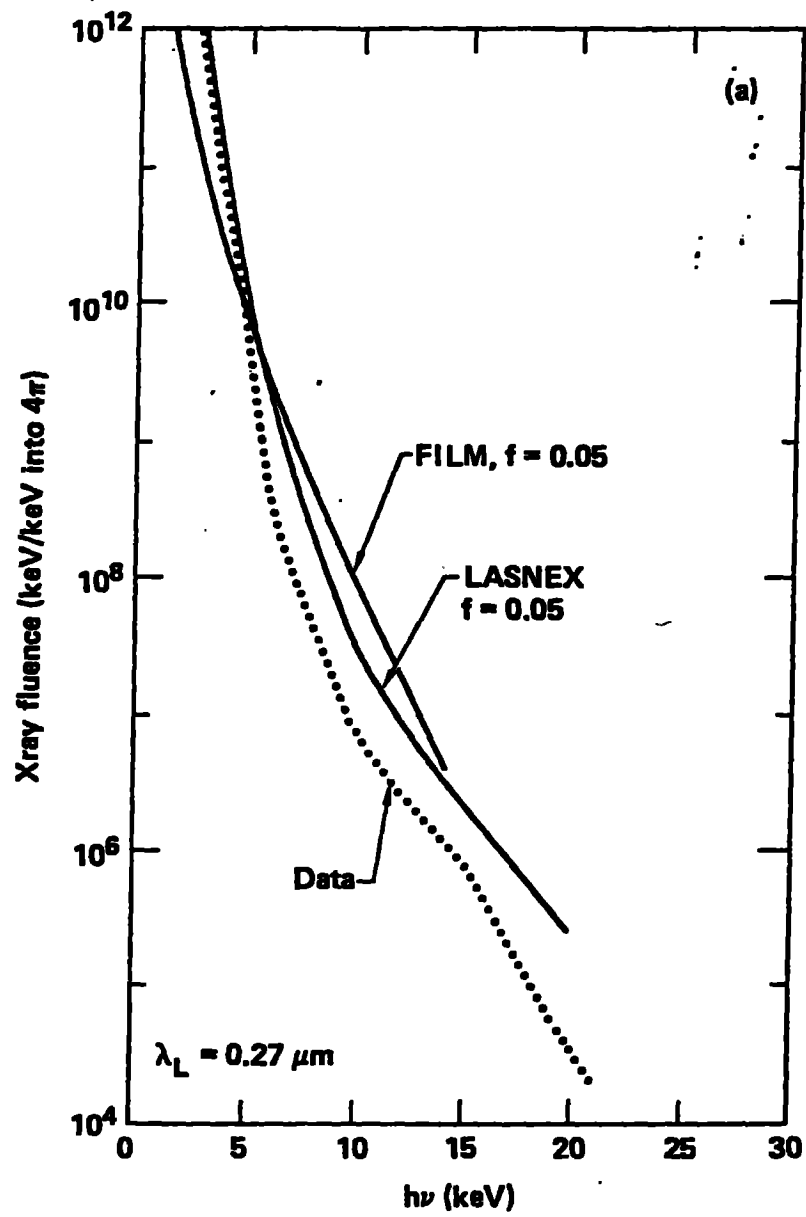


Fig. 11a

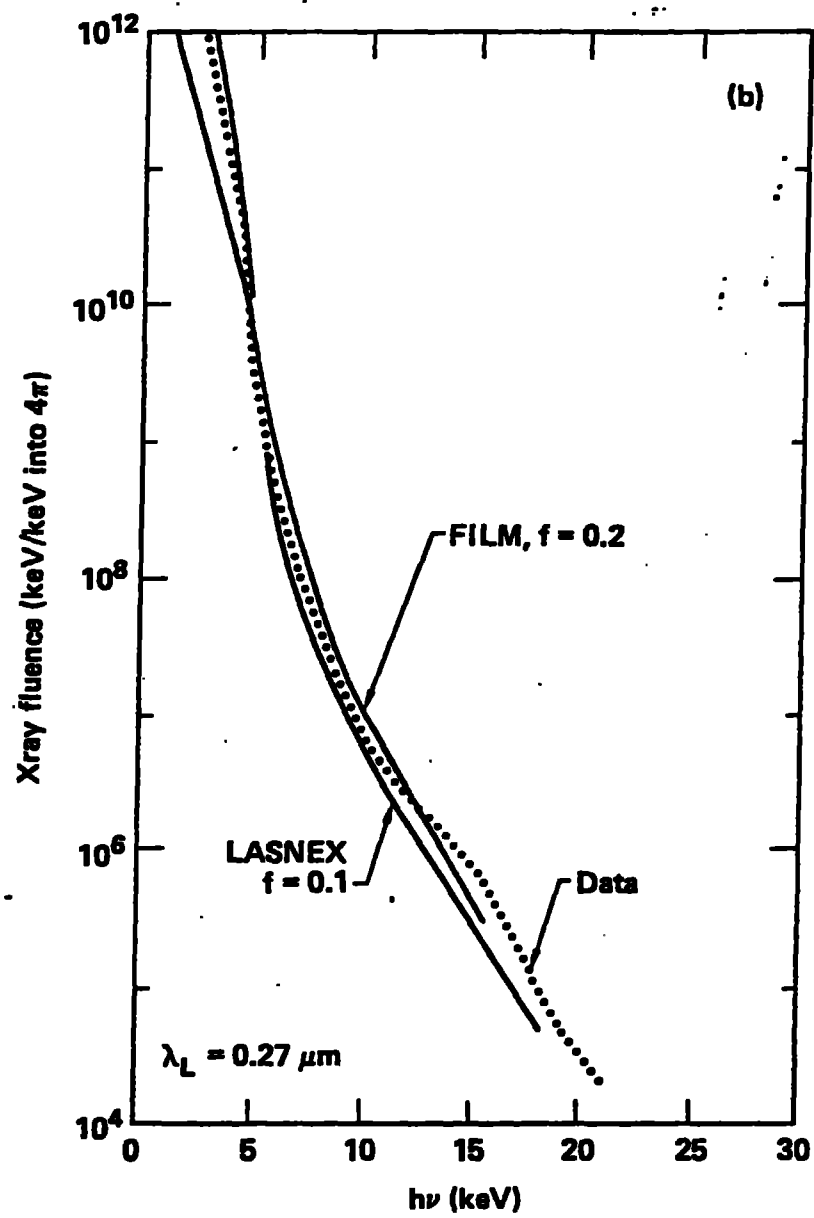


Fig. 11b

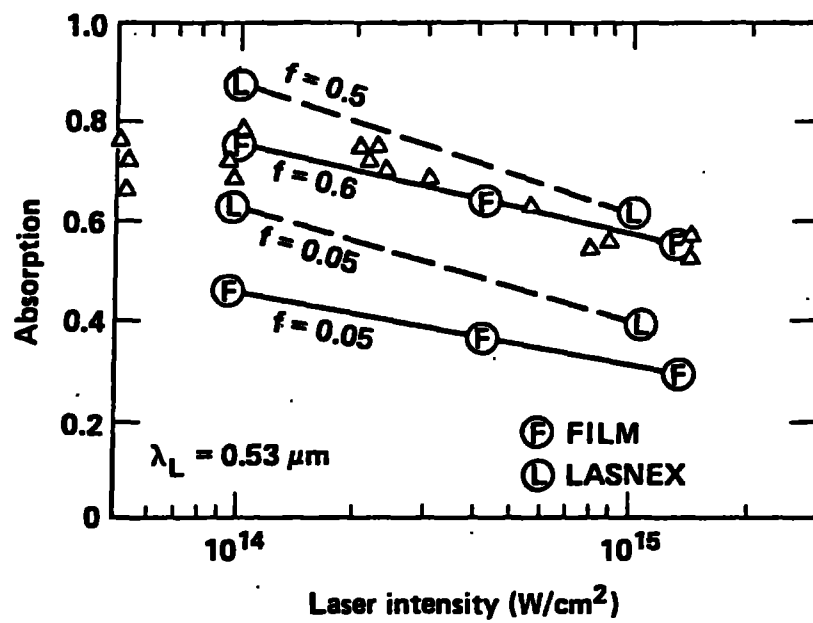


Fig. 12

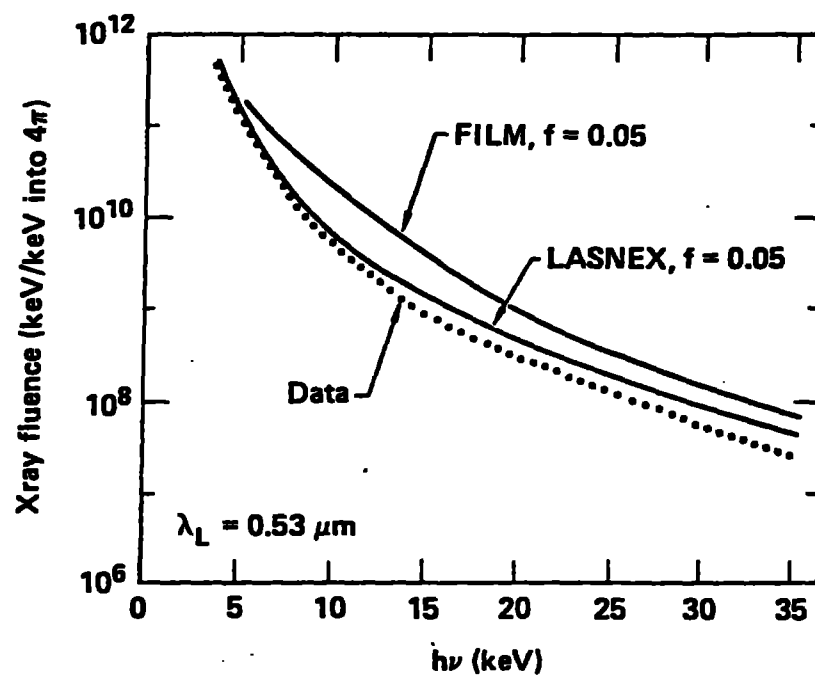


Fig. 13

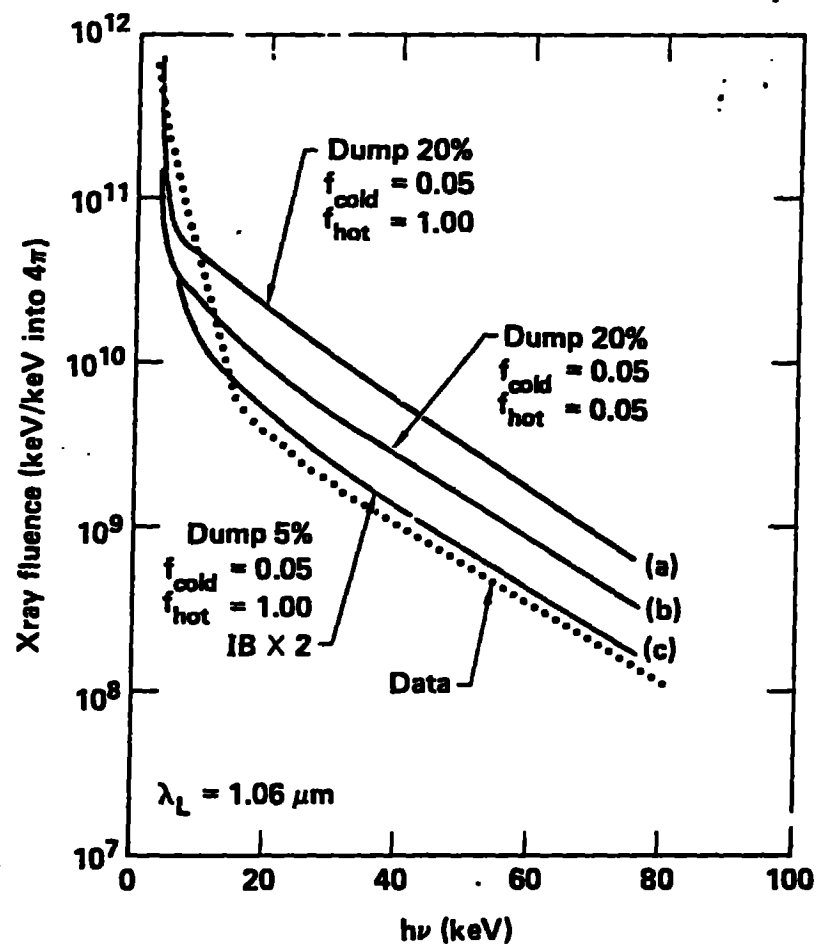


Fig. 14

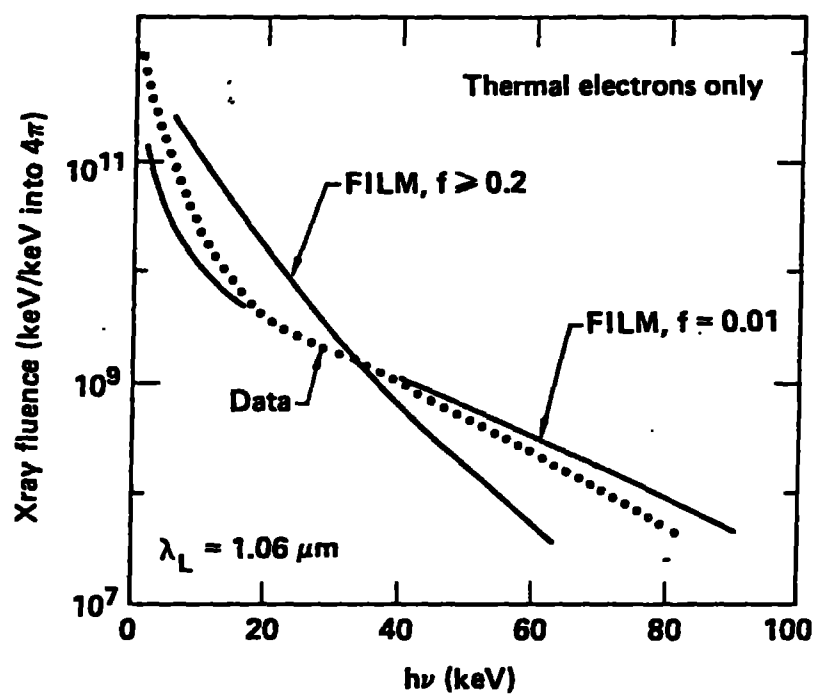


Fig. 15